https://doi.org/10.2352/ISSN.2470-1173.2020.15.COLOR-196

Data-bearing halftone image alignment and assessment on 3D surface*

Ziyi Zhao, Purdue University, West Lafayette, IN, USA
Yujian Xu, Purdue University, West Lafayette, IN, USA
Robert Ulichney, Hewlett-Packard Co., Stow, MA, USA
Matthew Gaubatz, Hewlett-Packard Co., Seattle, WA, USA
Stephen Pollard, Hewlett-Packard Co., Bristol, UK
Jan P. Allebach, Purdue University, West Lafayette, IN, USA

Abstract

An alignment approach for data-bearing halftone images, which are a visually pleasant alternative to barcodes, is proposed in this paper. In this paper, we address the alignment problem of data-bearing halftone images on a 3D surface. Different types of surfaces have been tested , using our proposed approach, and high accuracy results have been achieved. Additionally, we also develop a data retrieval tool from an aligned image, in order to decode the data embedded in the original image. A system to assess the accuracy of alignment is introduced to quantify the effectiveness of the proposed alignment approach.

Introduction

A data-bearing halftone image is a visually pleasant alternative to barcodes. The approach to embed data into halftone images and recover data from those images was proposed in [1]. A simple introduction of the data encoding system is that, for the first step, we generate a standard binary payload from the original binary payload. The standard payload is a circularly shifted version of the original payload that bears the smallest decimal value. For the next step, the standard payload is repeated across each row where for each row, the payload is circularly shifted by a fixed amount. An interleaving phase row is inserted periodically for the purpose of recording the shifting amount to recover the original payload from its standard payload. In this way, we generate a 2D data array from the encoding system. In the data recovery system, we need to determine the interleaving phase row first. After calculating the shifting amount of the payload from the determined phase row, we generate the payload from the data array, excluding the phase rows [2].

We also need to highlight how we embed the 2D data array generated from encoding system into a halftone image. A data-bearing halftone image consists of carrier cells, abstention cells and fiducial cells. A carrier cell is a halftone cell with a shifted dot cluster while an abstention cell is an empty halftone cell. The shifted dot cluster in a carrier cell represents a bit value in the 2D data array from encoding system. For example, if a dot cluster in a carrier cell shifts up or down, it indicates that the value in the corresponding position in the 2D data array is 1. If a dot cluster in a halftone cell shifts right or left, it indicates that the value in the corresponding position in the 2D data array is 0. A fiducial cell is a halftone cell with a non-shifted dot cluster. It doesn't carry any information, but is used for alignment. The detail of how the alignment approach uses fiducial cell rows will be introduced in the next section. Figure 1 is an example of a data-bearing halftone image.

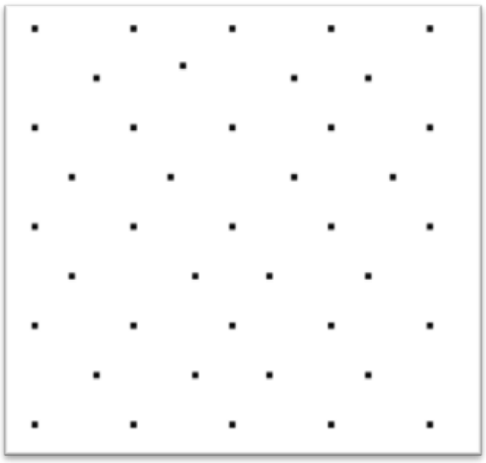

Figure 1. *An example of a portion of a data-bearing halftone image. The first, third, fifth, seventh, and ninth halftone cell rows are fiducial cell rows with a fixed dot cluster in each fiducial cell. In each row, the fiducial cells alternate with abstention cells that are empty. The second, fourth, sixth, and eighth rows are carrier and abstention cell rows where a shifted dot cluster is in each carrier cell, which alternate with empty cells thatv are abstention cells.*

Overview of Alignment Approach on a 2D Surface

As an alternative to a frequency domain peak based alignment approach [3], [4], [5], an alignment approach based on grid finding and expanding on a flat 2D surface was proposed in [6]. The procedure can be described as follows: After capturing the printed page, we are able to acquire the difference image from two filtered images generated by applying two different kernels of a Gaussian filter to the captured image. Then, we detect all the candidate dot clusters in this Gaussian difference image. Next, we find all crossings in the captured image. A crossing is formed by 5 fiducial dot clusters. Since the dot cluster is fixed in a fiducial cell, the line formed by east-center-west fiducial dot clusters should be

*Research supported by HP Labs, Palo Alto, CA 94304.

perpendicular to the line formed by north-center-south fiducial dot clusters. Then, we find the connected crossings that share some of the same dot clusters. Among all the connected crossings, we find a connected crossing which has the largest number of crossings as the best segment. Then, we generate an initial grid which covers all the dot clusters in the best segment. Finally, we expand that grid to the entire image. Figures 2-8 show the steps of this approach.

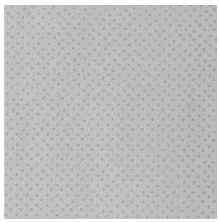

Figure 2. *Captured Image.*

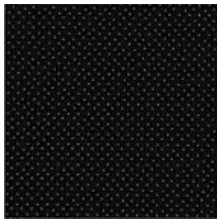

Figure 3. *Difference Image.*

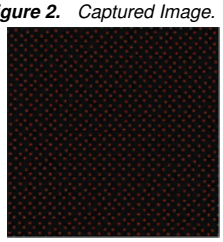

Figure 4. *Detected Dot Clusters (red).*

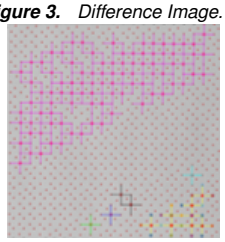

Figure 5. *Crossings (pink, purple, blue, green...).*

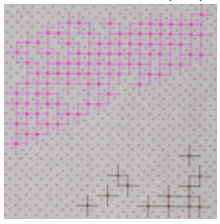

Figure 6. *Largest Connected Crossings (pink).*

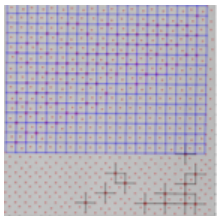

Figure 7. *Initial Grid (blue).*

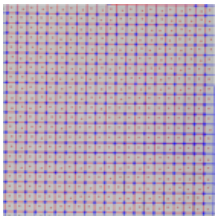

Figure 8. *Expanded Grid (blue).*

Alignment Approach on 3D Surfaces

We tested this alignment approach on two types of 3D surface. One surface is an oblique planar surface, while the other surface is a cylindrical surface. The alignment approach is different for these different types of surfaces.

Alignment Approach and Experimental Test Setup for an Planar Oblique Surface

We use the same alignment approach introduced in the last section for an oblique surface. A video capture device is fixed on a column while a printed page is attached to an oblique surface. The printed page can be rotated on the oblique surface and the elevation angle of the surface can also be varied. The experimental setting is shown in Figure 9.

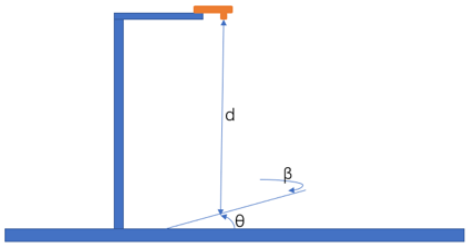

Figure 9. *The printed encoded halftone page is placed on an oblique surface directly beneath the video camera at a distance d along the optical axis of the camera. In this setting, we can modify d, the azimuth angle β of the halftone page with respect to the field of view of the camera, and the angle θ of elevation of the oblique surface with respect to the base platform.*

Alignment Approach and Experimental Test Setup for a Cylindrical Surface

The alignment approach applied on a cylindrical surface is different from the approach in the last section, as the cylindrical surface is not flat. It is very hard to directly apply the previously described grid finding approach to the image of the cylindrical surface. To address this issue, we divide the captured image into several sub-images. When the sub-images are small enough, the cylindrical surfaces within these sub-images are nearly planar. So, we can apply the previously described grid finding approach on such sub-images. Thus, we propose an approach to divide the image into sub-images and merge them into one image after alignment. We test the method on cylindrical surfaces, but it can be extended to other surfaces.

An assumption that we make is that the number of fiducial dot clusters should be the same as the number of carrier dot clusters. For example, in Figure 1, the number of carrier dot clusters and the number of fiducial dot clusters are almost the same for such a checkerboard distribution. Below are the steps of the alignment approach that we follow:

1. For a 1920 $\times$ 1080 captured image, we segment the image into N $\times$ N sub-images. Each sub-image has 50% percent overlapping with its neighbor sub-images. In this experiment, we choose N = 100 or 120

2. We align each sub-image separately using the grid finding alignment procedure described in the last section

3. Next, we find the most aligned sub-image. The most aligned image is defined as the sub-image in which the ratio of the number of determined fiducial dot clusters and the number of determined carrier dot clusters is closest to 1.0 according to the assumption we made above.

4. Finally, we expand the generated grid in this most aligned image to its neighboring sub-images using the overlapping region between neighboring sub-images until the grid covers the entire image. The expanding sequence is based on a Breadth First Search (BFS). The expanding details across neighboring sub-images will be introduced in the next section.

Grid Expanding Technique within a Sub-image

In the alignment approach on a 2D planar surface, we find all the crossings and determine the best connected crossing segment that has the largest number of connected crossings (Figure 6). A feature of a crossing is that within a crossing, the relative position of the five dot clusters are determined. The five dot clusters are in the north, south, west, east, and center positions in the crossing. In terms of relative positions of dot clusters, a relative position coordinate system is developed over the entire image. In the mean time, we also have a real pixel-wise image coordinate system. Thus, a homography is built to map from the real pixel-wise image coordinate system to the relative position coordinate system [7].

$$Coord_{relative-position} = H \cdot Coord_{pixel-wise-position} \quad (1)$$

Figure 10 is an example of relative coordinate and image pixel-wise coordinate system.

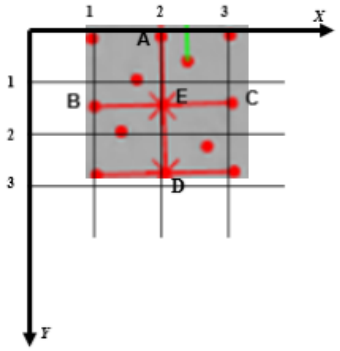

Figure 10. *Illustraion of relation between relative coordinate and image pixel-wise coordinate systems. In the plot, A(2.0, 0.0), B(1.0, 1.5), C(3.0, 1.4), D(2.0, 2.8), E(2.1, 1.4). This is in the real pixel-wise coordinate system consistent with the axes in the plot. As A, B, C, D, E are in one crossing, their coordinates in the relative coordinate system are B(-1, 0), E(0, 0), C(1, 0), A(0, -1), D(0, 1). This coordinate system records their locations relative to dot cluster E.*

Thus, in order to expand the grid in this sub-image, we need to obtain a homography between the determined fiducial dot clusters' relative position coordinate system and real image coordinate system. Then we expand the relative position image to cover the entire sub-image, and finally, map back to the real image coordinate system. Ideally, in the real image coordinate system, there should be dot clusters near the vertices of the expanded real image system grid. As long as there is a dot cluster close to the expected dot cluster position, we will classify it as latest determined fidcual dot cluster. The expanding process is shown in Figures 7 and 8.

Grid Expanding Technique Across Sub-images Based on Breadth First Search

From Step 4, we need to find the most aligned sub-image among all sub-images. Then we need to expand the grid across the sub-images. The expanding order is based on a Breadth First Search (BFS) [8]. Now, we imagine that all the sub-images are vertices in a graph. The expanding order will be Breadth First Traversal of the graph from the initial vertex, which is the most aligned image. An example is shown in Figure 11. We define the sub-image with grids to be generated as the target image. The sub-image, with generated grids, is defined as a reference image. In Figure 11, suppose that the most aligned image is sub-image index 14. In order to expand the generated grid in the target sub-image 8, we first find all the neighbor images of target image 8 which are sub-images 9, 14, 13, 12, 7, 2, 3, 4. Among all these sub-images, we use those in which the grid has already been generated as reference images. They are 9, 14, 13. (Please note that there are overlapping regions between sub-images, which isn't reflected in the plots). In sub-images 9, 13, 14, as the grid is already generated, the fiducial dot clusters are determined as well. Those fiducial dot clusters in the overlapping regions in sub-image 8 and sub-images 9, 13, 14 are then used to generate a new grid within sub-image 8 using the technique described in the previous section. In the new generated grid in sub-image 8, we find whether there are some dot clusters that are close to the grid. If so, these dot clusters are classified as the latest fiducial dot clusters. In this way, the grid is expanded into sub-image 8 from sub-images 9, 13, 14.

Figure 11. *BFS traversal sequence (root = 14). Suppose that the most aligned sub-image is index 14, then we expand the grid to indices 9, 13, 15, 19, then to 4, 8, 10, 12, 18, 20, 24 ...*

Data retrieval tool

Once we determine the fiducial dot clusters in the entire image, we can classify the remaining dot clusters as carrier dot clusters. As mentioned above, there is a relative position system in the image. The global relative position system is shown in Figure 12. Moreover, we also have a global pixel-wise image coordinate system. Thus, we can calculate the homography mapping from pixel-wise image coordinates to relative position coordinates. Once this homography is obtained, we can calculate the relative position for each carrier dot cluster based on its pixel-wise image position. The relative position of each carrier dot cluster indicates the shifting direction of the carrier dot cluster towards its four surrounding fiducial dot clusters. Thus, we can recover the 2D data array from all determined carrier dot clusters.

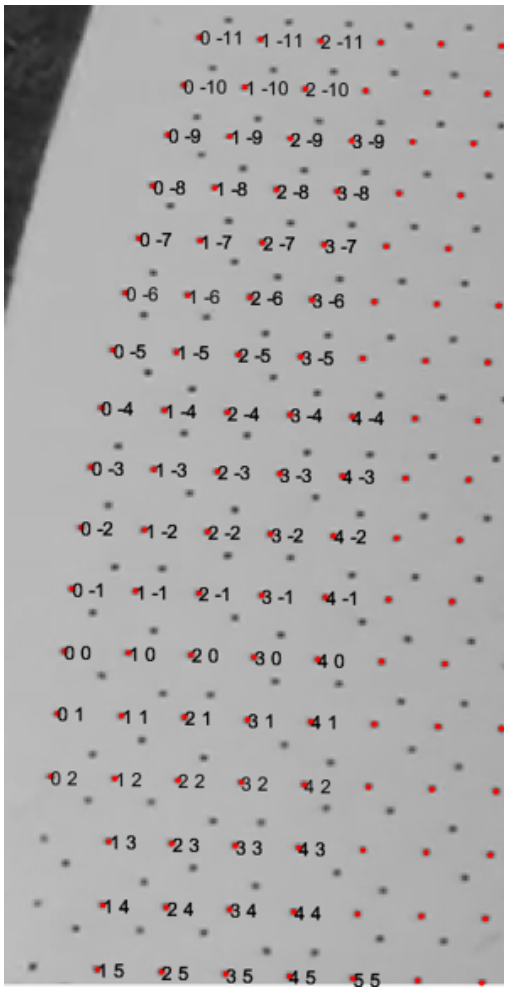

Figure 12. *Zoom-in of Global Relative Position Corrdinate System in an image. There are two numbers beside each red dot cluster. The 1st number is the relative position index along the column, and the 2nd number is the relative position index along the row. The position indices are relative to the position of the leftmost fiducial dot cluster on the sixth row from the bottom of the image, which has the label 0 0.*

Results

In this section, we will show some qualitative and quantitative results to prove the effectiveness of our alignment approach.

Qualitative Results for Alignment on an Oblique Planar Surface

The qualitative result is shown in Figure 13. The grid lines in red are drawn from the determined fiducial dot clusters (The blue dot clusters at the intersection of the grid lines are fiducials). The blue stars are the selected connected crossings that were used to generate the initial grid while green stars are other crossings. From the figure, we can clearly observe that the grid is generated successfully.

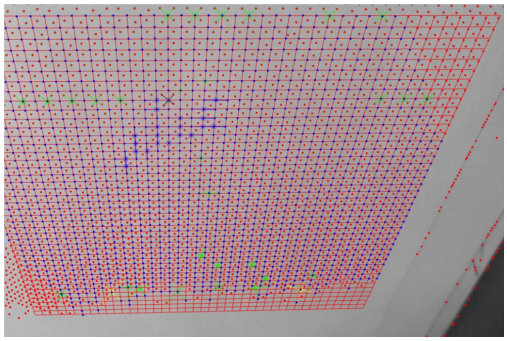

Figure 13. *Grid generated on an oblique planar surface after applying our alignment approach. The green, yellow, blue, and black lines are the detected candidate crossings. We finally use the blue connected crossings (also labeled with blue star) as our initial grid.*

Qualitative Results for Alignment on a Cylindrical Surface

The qualitative result for a cylindrical surface is shown in Figures 14 and 15. Figure 14 shows the detected dot clusters (in blue) on the cylindrical surface. Note that the carrier dot clusters and fiducial dot clusters are not classified in this figure. Figure 15 shows the result of the classified fiducial dot clusters (in red) after applying our approach. The results shows that most of fiducial dot clusters are classified correctly.

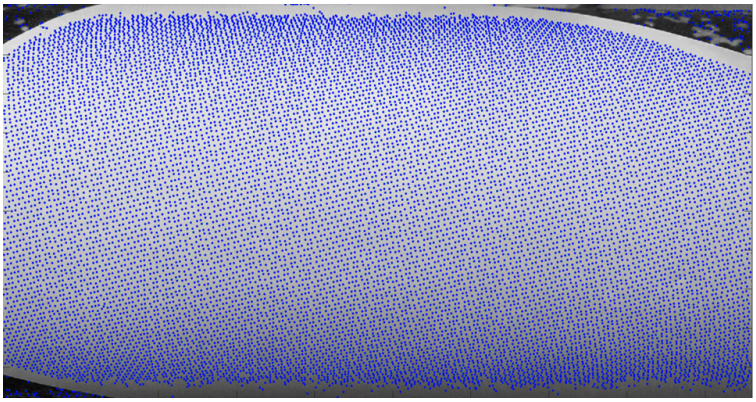

Figure 14. *Detected dot clusters (in blue) without classification.*

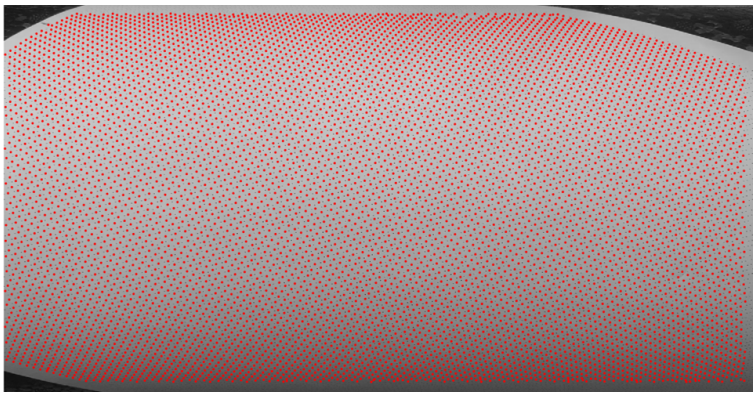

Figure 15. *Classified fiducial dot clusters (in red) after using our approach.*

Quantitative Assessment of Alignment

In the previous section, we have provided some qualitative results of our alignment approach applied to an oblique planar surface and a cylindrical surface. However, this is far from enough, as we want to develop a scheme to quantify the results from our approach, so that we can determine whether the approach improves if we change it in the future.

Specifically, our goal is to determine, in different regions of a cylindrical surface, how many fiducial dot clusters are classified correctly. This leads to one issue to complete this quantifying process. The issue is how to define these regions on a cylindrical surface. Thus, in order to solve this, we propose a technique that is introduced in the next section.

Reference Image Boundary Technique

In this section, our purpose is to solve the issue of region separation on the cylindrical surface. There are two potential methods to divide the regions. One is that we print a set of boundaries on the data-bearing halftone images so that we can find the boundaries in the captured images and then locate the determined fiducial dot clusters in each region separated by these boundaries. The other method is that we print reference boundaries on a blank page. We decided to adopt the second method, which is printing the boundaries on a blank page. The reason is that if we directly print boundaries on the page containing the halftone image, the boundaries printed on the page may cover some dot clusters in the data-bearing halftone image.

Thus, we print the boundaries on a blank page. The procedure is as follows: First, we fix the printed page (data-bearing halftone image without boundaries) on our mounting fixture and capture the image using a video capture device. Then, we use the blank page with printed boundaries and fix it on the same mounting fixture that we used for the page with the data-bearing halftone image. Note that we need to fix the reference boundary blank page at the exact same place as where the previous printed data-bearing halftone was located. Examples are shown in Figures 16 and 17.

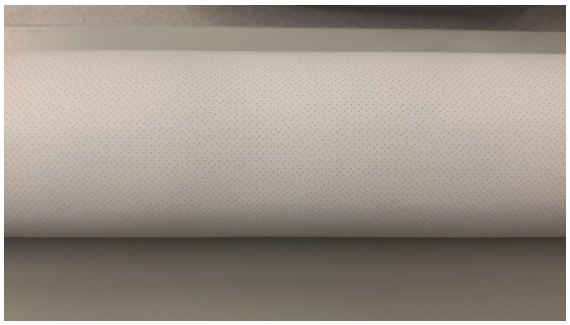

Figure 16. *Captured image of printed data-bearing halftone page.*

After collecting videos from these two pages, we need to detect the boundaries using image processing techniques. Below are the steps in the detection process:

1. Transfer the image of the reference page from RGB to HSV: We select the red elements in the HSV image from the hue channel.

2. Manually choose one column which crosses all horizontal reference lines. Input that column X coordinate to the program (Figure 18).

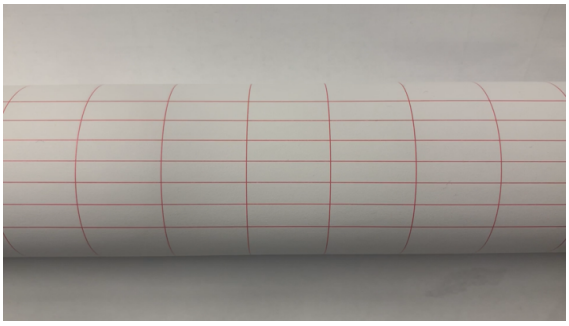

Figure 17. *Captured image of printed reference page with boundaries.*

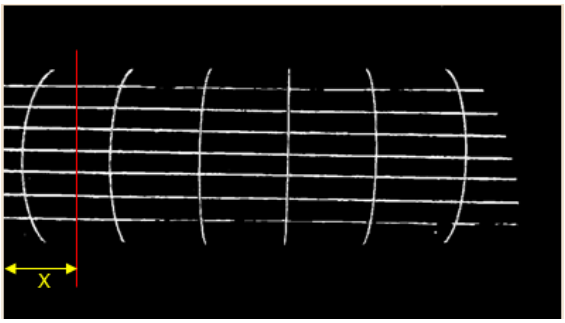

Figure 18. *Process for establishing regions in the reference image within which the accuracy of the grid alignment method may be locally evaluated. Manually choose a column X that crosses all the horizontal reference lines*

3. Dilate and erode the image. We use Equation 2 for dilation operation while we use Equation 3 for erosion operation

$$X \oplus H = \{(x,y) : H_{(x,y)} \cap X \neq \emptyset\} \tag{2}$$

$$X \ominus H = \{(x,y) : H_{(x,y)} \subseteq X\} \tag{3}$$

Where X is the original image, $H \subseteq R^2$ *or* Z^2 is the structuring element, and $H_{(x,y)}$ is the translate of the set H by the vector $(x,y) \in R^2$ *or* Z^2. In our case, structure element H is 3×3 square.

4. Along the Y axis (vertically), we record the sum value of pixels for each Y value. For each Y value, if its sum pixel value exceeds a threshold, we count it as 1, or it is 0. In this way, we can find the horizontal reference line. Then, we reset the sum to 0, and continue the count in order to find the next horizontal reference line.

5. For each reference line (horizontal), we record the Y value of its top side and bottom side. Based on this, we acquire the interval between the horizontal reference lines

6. To detect vertical lines, we take advantage of the fact that we have already acquired the horizontal reference line intervals. So we look into each interval separately. For example, in the first interval, we choose the mid line in the first interval as the starting line. We use the same method as in the previous step. Specifically, we choose its neighboring lines and record its variation along X

axis. So that we can expand the vertical reference line in this interval.

7. For the other intervals, we do the same procedure.

In this way, we determine all the reference lines, as shown in Figures 19 and 20.

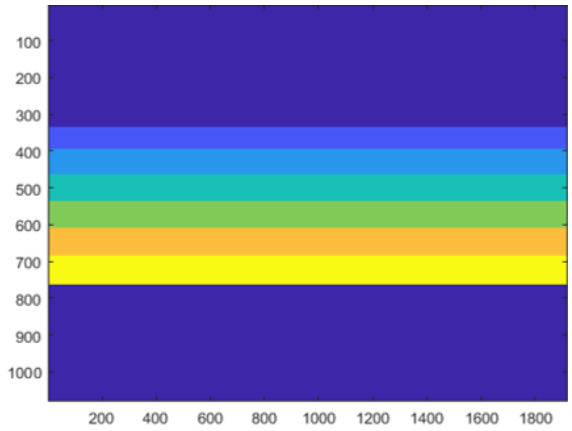

Figure 19. *Detection of horizontal reference lines.*

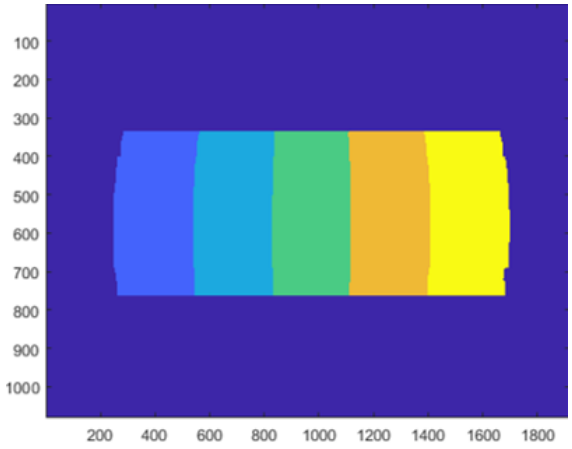

Figure 20. *Detection of vertical reference lines.*

Quantitative Result of Alignment on Cylindrical Surface

We perform the experiments using the setup shown in Figure 9. The parameter values that we choose for this experiment are as follows: The distance from the camera to the printed page is 6 *in*; the radius of cylinder is 2 *in* and the angle between the horizontal lines on the printed page and the major axis of the cylinder is 0° . Below is the result of our alignment method.

Table 1. The fraction of correctly classified fiducial dot clusters in different regions of the printed page on the cylinder (*R* is the radius of the cylinder)

Vertical Distance \ Horizontal distance	*-R* - *R*/2	*-R*/2 - 0	0 - *R*/2	*R*/2 - *R*	*R* - 3/2*R*
-R - 3*R*/4	0.72	0.71	0.90	0.96	0.82
-3*R*/4 - -2*R*/4	0.96	0.94	0.93	0.90	0.92
-2*R*/4 - -*R*/4	0.93	0.93	0.92	0.93	0.97
-*R*/4 - 0	0.92	0.89	0.91	0.89	0.93
0 - *R*/4	0.92	0.91	0.93	0.98	0.97
R/4 - 2*R*/4	1.0	0.91	0.97	0.95	0.90
2*R*/4 - 3*R*/4	0.94	0.88	0.96	0.92	0.94
3*R*/4 - *R*	0.69	0.63	0.83	0.65	0.68

From Table 1, we see that in most regions in the printed page, the rate of correctly classified fiducial dot clusters is over 90%. The rate generally decreases at the border regions of the cylinder. However, it still achieves a high accuracy. This result proves the robustness and effectiveness of our approach.

Conclusion

In this paper, we proposed an approach to solve the issues for the 3D alignment of data bearing halftone images. High accuracy of data recovery is achieved using our approach. Additionally, we also developed a tool to quantify our result.

References

[1] R. Ulichney, M. Gaubatz, and S. Simske, Encoding information in clustered-dot halftones, NIP & Digital Fabrication Conference. Society for Imaging Science and Technology, vol. 2010, pg. 602. (2010).

[2] R. Ulichney, M. Gaubatz, and S. Simske, Circular coding for data embedding, NIP & Digital Fabrication Conference. Society for Imaging Science and Technology, vol. 2013, pg. 142. (2013).

[3] S. Pollard, R. Ulichney, M. Gaubatz, Recovering planar projection of printed cluster-dot halftones, IEEE International Conference on Image Processing. (2014).

[4] C-J. Tai, R. Ulichney, and J. P. Allebach, Effect on Fourier Peaks Used for Periodic Pattern Detection. Color Imaging XXI: Displaying, Processing, Hardcopy, and Applications, (Part of IS&T Electronic Imaging 2016), R.Eschbach, G. G. Marcu and A. Rizzi, Eds. San Francisco, CA, 14-18 February 2016.

[5] Z. Zhao, R. Ulichney, M. Gaubatz, S. Pollard, J. Allebach, Advances in the Decoding of Data-Bearing Halftone Images. NIP & Digital Fabrication Conference. Vol. 2019. No. 1. Society for Imaging Science and Technology, 2019.

[6] S. Pollard, S. Simiske, G. Adams, Digital signature authentication, US Patent 10,558,879

[7] E. Artin, Geometric Algebra, Interscience Publishers, 1957

[8] H. Cormen, C. Leiserson, R. Rivest, and C. Stein, Introduction to Algorithms, Second Edition. MIT Press and McGraw-Hill, 2001

Author Biography

Ziyi Zhao received his BS in Naval Architecture and Ocean Engineering from Shanghai JiaoTong University from China (2015). He is currently a PhD student, working as an image processing research assistant with Prof. Jan Allebach, in the School of Electrical and Computer Engineering at Purdue University. His research interests are in image information embedding and digital image security, etc. He has been working on the project of circular coding sponsored by HP Labs.

JOIN US AT THE NEXT EI!

IS&T International Symposium on

Electronic Imaging

SCIENCE AND TECHNOLOGY

Imaging across applications . . . Where industry and academia meet!

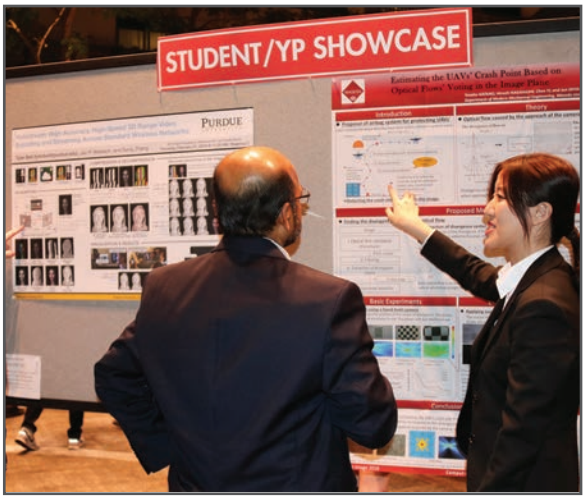

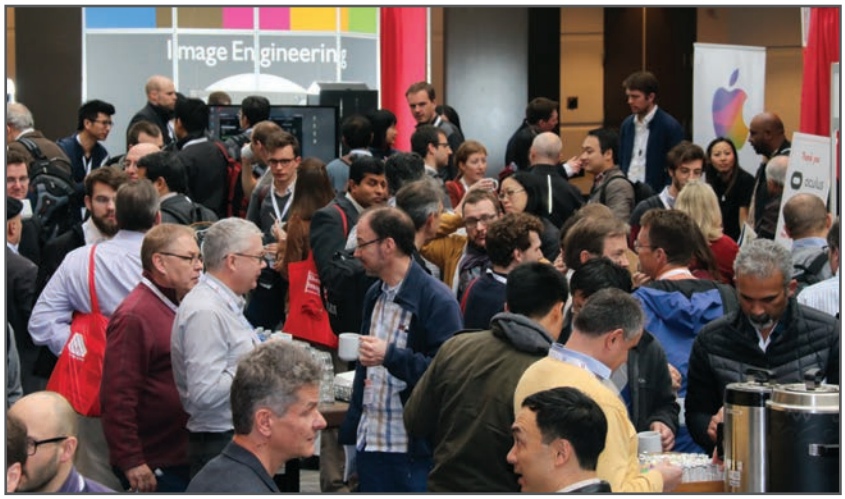

• SHORT COURSES • EXHIBITS • DEMONSTRATION SESSION • PLENARY TALKS •
• INTERACTIVE PAPER SESSION • SPECIAL EVENTS • TECHNICAL SESSIONS •

www.electronicimaging.org

IS&T
imaging.org